IMPACTS OF DIFFERENT FACTORS ON SEEPAGE AND LAND UPLIFT DUE TO COMPRESSED-AIR INJECTION

Zang Yongge
Tianjin University,
State Key Laboratory of Hydraulic Engineering Simulation and Safety
Tianjin 300072, China
E-mail: zangyongge2011@163.com

Sun Dongmei *(corresponding author)*
Tianjin University,
State Key Laboratory of Hydraulic Engineering Simulation and Safety
Tianjin 300072, China
E-mail: sundongmei@tju.edu.cn

Feng Ping
Tianjin University,
State Key Laboratory of Hydraulic Engineering Simulation and Safety
Tianjin 300072, China
E-mail: fengping@tju.edu.cn

Stephan Semprich
Graz University of Technology,
Institute of Soil Mechanics and Foundation Engineering
8010 Graz, Austria
E-mail: stephan.semprich@tugraz.at

Keywords

loosely coupled two-phase flow and geo-mechanical model; in-situ, air-flow test; compressed-air injection; multiphase flow; land uplift; air loss

Abstract

In this study, using an in-situ, air-flow test in Essen, the impacts of different factors on multiphase flow and land uplift during and after compressed-air injection were investigated using numerical simulations. A loosely coupled, two-phase flow and geo-mechanical modeling approach, linking two numerical codes (TOUGH2/EOS3 and FLAC^{3D}) was employed to simulate the in-situ, air-flow test for comparing the simulated and measured results. As the compressed air is injected, it flows upwards and laterally, and the vertical effective stress near and above the injection zones decreases owing to the pore pressure increasing here, causing an expansion of the soil skeleton in the corresponding zones. The land uplift, induced mainly by support actions from lower deformed soils, is relevant to the distribution of the porosity increments in the soil interior, and it increases rapidly during air injection. After the compressed-air injection stops, the land uplift decreases gradually to zero due to the overpressure dissipation. With a combination of intensive rainfall, the land uplift is slightly greater near the borehole, but it is significantly greater at a distance from the borehole than the land uplift with no or low rainfall, but the air-injection rate remains almost unchanged due to the unchangeable pore pressure near the injection region. As the intrinsic permeability increases or the air entry pressure decreases in the injected strata, both the land uplift and the air-injection rate increase, but the time required for the land uplift to become zero is slightly advanced with either a small permeability or a high air entry pressure.

1 INTRODUCTION

During tunnel construction below the groundwater table, due to the relatively higher groundwater pressure and the greater hydraulic conductivity, the pore-water in soil voids flows into the work space through the excavated surface, which may hinder the progress of the construction or even cause the collapse of the tunnel. It would, therefore, be advantageous to apply the compressed-air technique during the tunnel's construction [1-2]. By introducing pressurized air into the tunnel space, the groundwater inflow through the excavated surface could be prevented and the surface settlement can also be reduced, which is very critical in an urban area where the damage of settlements on the existing buildings must be concerned. It is important to note that the applied compressed-air pressure in the tunnel space must be equal to or greater than the magnitude of the groundwater pressure at the tunnel invert, so that the compressed air can permeate into the surrounding soils due to the pressure gradient. In

addition to this application, subsurface fluid injection has been applied extensively for energy development and environmental management, such as enhancing oil production, storing useful gas or oil in depleted gas/oil fields, recharging an over-drafted aquifer system, arresting or mitigating land subsidence, and disposing of contaminants and hazardous wastes, and other applications [3-6].

Actually, these applications of pressurized fluid injection all involve an interaction between multiphase fluid flow and geo-mechanical processes, and they could affect the variation of the seepage and the stress state in the porous media [5, 7-9]. The simultaneous consideration of the gas phase, liquid phase, and solid phase underground could therefore produce a more realistic result. Numerical analyses, compared to analytical solutions, can dispose of the complicated initial and boundary conditions, the multi-layered soils and the complex geometry of many engineering problems, and is a better choice to analyze the coupling processes between multiphase fluid flows and soil deformation. Selvadurai and Kim developed a mathematical solution to study the caprock-storage formation interactions during the injection of fluids into a poroelastic storage formation and the ground subsidence caused by the uniform extraction of fluids from a disc-shaped region [10-11]. A loosely coupled methodology, linking two numerical codes (TOUGH2, used for solving multi-phase multi-component flow equations [12]; and FLAC^{3D}, used for solving geo-mechanical, stress-strain equations [13]), was proposed by Rutqvist et al. [14] and Rutqvist and Tsang [15] to simulate the interactive processes between the geo-mechanical and fluid-flow processes. This coupled simulator has been widely applied in many geo-environmental situations, such as nuclear waste disposal, CO_2 sequestration, geothermal energy extraction, naturally occurring CO_2 upwelling with surface deformations, and gas production from hydrate-bearing sediments [16-20].

Therefore, in this study, on the platform of the in-situ, air-flow test in Essen conducted by Kramer and Semprich [1], the water-air, two-phase flow processes and soil deformation during and after compressed-air injection were investigated using the coupled TOUGH2-FLAC^{3D} simulator. Notably, the in-situ, air-flow test was carried out to explore the behavior of the outcropping soils before the subway construction using the compressed-air technique in Essen, Germany. Then, the impacts of the different factors on the multiphase flow and land uplift during and after compressed-air injection were analyzed, including the occurrence of a rain event, and a sensibility analysis of the values of the permeability and air entry pressure of the injected strata.

2 COUPLING PROCEDURES

TOUGH2/EOS3 is a module in TOUGH2 for non-isothermal, water-air, two-phase flow in three-dimensional, unsaturated-saturated porous and fractured media, in which the transformation and dissolution processes occurring between the liquid and gas phases are explained by mass-balance equations. These balance equations are discretized in space by the integral finite difference and in time by the first-order finite difference. FLAC^{3D} is a three-dimensional and explicit finite-difference computer code for solving geo-mechanical stress-strain equations. In the coupled two-phase flow and geo-mechanical process, the seepage process affects the stress field by changing the pore pressure and the effective stress, whereas the stress field affects the seepage through changing the porosity, the capillary pressure and the intrinsic permeability.

2.1 Update of Geo-mechanical Variables

In the loosely coupled procedure, the pore water pressure p_l, the pore air pressure p_g, and the liquid saturation S_l provided by TOUGH2 (the pore pressure is referred to the local atmospheric pressure, and the same below) are sent to FLAC^{3D} to calculate the average pore pressure p[14]:

$$p = S_l p_l + (1 - S_l) p_g \qquad (1)$$

This expression for the average pore pressure is applied to porous sedimentary rock [14, 21], and the medium was assumed to be porous media in this study. Then, the average pore pressure is incorporated into the calculations of the soil skeleton stress, the strain, and the effective stress σ_{ij}' ($\sigma_{ij}' = \sigma_{ij} - p\delta_{ij}$, where σ_{ij}' is the total stress and δ_{ij} is the Kronecker function (for $i = j$, $\delta_{ij} = 1$; for $i \neq j$, $\delta_{ij} = 0$)). The change in porosity $d\phi$ induced by the soil deformation can be expressed as follows:

$$\begin{aligned} d\phi = d(V_p / V_t) = (V_t dV_p - V_p dV_t) / V_t^2 = \\ = dV_p / V_t - \phi_0 dV_t / V_t \end{aligned} \qquad (2)$$

where V_p is the pore volume, V_t is the total volume, and ϕ_0 is the initial porosity at the initial stress. The total volume V_t is equal to the sum of the pore volume V_p and the solid grain volume V_s. Here, it is assumed that the deformation of the solid grains is much less than that of the soil skeleton, and can be negligible. Therefore, the change in the total volume V_t is equal to the change in the pore volume V_p, i.e., $dV_t = dV_p$, and the change in porosity $d\phi$ can be given by

$$d\phi = (1 - \phi_0) dV_t / V_t = (1 - \phi_0) \varepsilon_v \qquad (3)$$

where ε_v is the volumetric strain.

2.2 Update of Hydraulic Variables

The geo-mechanically induced $d\phi$ has an immediate effect on the fluid flow behavior, including the intrinsic permeability and the capillary pressure. The Kozeny-Carman Equation suggests that there should be a linear relation between the hydraulic conductivity k (or the intrinsic permeability K, $k = K\gamma_w / \mu_w$, where γ_w is the unit weight of water and μ_w is the dynamic viscosity of water) and $e^3/(1+e)$ (or $\phi^3/(1-\phi)^2$, where e is the void ratio and ϕ is the porosity) of porous materials. Furthermore, according to Chapuis and Aubertin [22], the Kozeny-Carman Equation predicts the hydraulic conductivity of most soils (for 10^{-1} to 10^{-11} m/s) fairly well and can be applied to the soils encountered in this study. Hence, for a given soil, the ratio of the intrinsic permeability $K_n(\phi_n)$ at the time step n to the initial intrinsic permeability $K_0(\phi_0)$ can be expressed as follows:

$$\frac{K_n}{K_0} = \frac{\phi_n^3 / (1-\phi_n)^2}{\phi_0^3 / (1-\phi_0)^2} \qquad (4)$$

where ϕ_n is the porosity at the time step n. Therefore, the intrinsic permeability K_n at the time step n can be defined with Eq. (5). This relationship has also been used by Taylor to estimate the unknown hydraulic conductivity at a porosity from a known hydraulic conductivity at another porosity for the same soil [23].

$$K_n = K_0 \left(\frac{\phi_n}{\phi_0} \right)^3 \left(\frac{1-\phi_0}{1-\phi_n} \right)^2 \qquad (5)$$

According to Rutqvist and Tsang [15], with respect to porous media, the capillary pressure is scaled with the intrinsic permeability and porosity according to a function by Leverett [24].

$$p_{cLn} = p_{cn} \frac{\sqrt{K_0 / \phi_0}}{\sqrt{K_n / \phi_n}} \qquad (6)$$

where p_{cLn} is the corrected capillary pressure at the time step n and p_{cn} is the calculated capillary pressure dependent on the liquid saturation at the time step n.

2.3 Coupling Procedure

The loosely coupling process between TOUGH2 and FLAC^{3D} is typically developed according to the procedure in Fig.1. Some input data files for TOUGH2 and FLAC^{3D}, such as the soil properties, mesh, boundary and initial conditions, must be initially prepared. Then TOUGH2 is executed for a sufficient simulation time to obtain an initial steady state, and FLAC^{3D} is also operated under gravitational loads to establish initial equilibrium stress gradients and outputs the initial porosity ϕ_0 of each element. Hereafter, the coupling process of TOUGH2-FLAC^{3D} starts. The initial porosity ϕ_0 from the FLAC^{3D} element is mapped to the TOUGH2 element, which is used to update the intrinsic permeability according to Eq.5. TOUGH2 is firstly executed for the first time-step, and the capillary pressure is corrected using Eq.6. When convergence is reached at the end of this time-step, the pore water pressure p_l , the pore air pressure p_g , and the liquid saturation S_l of each element in TOUGH2 are obtained and are mapped to the FLAC^{3D} nodes using a weighted distance interpolation. Then FLAC^{3D} runs under loads of average pore pressure for each node (which can be calculated using Eq.1), until an equilibrium state is reached. At this point the change in the porosity at the FLAC^{3D} element can be calculated according to the strain increment (by Eq.3). Afterwards, the updated porosity at the FLAC^{3D} element is sent back to the TOUGH2 element by interpolation. Utilizing the updated porosity, the intrinsic permeability is updated again according to Eq.5, and TOUGH2 is executed for the next time-step. And then the above coupling processes are repeated until the specified simulation time (Sum-time) is reached.

3 EXPERIMENT AND NUMERICAL SIMULATION OF THE IN-SITU AIR-FLOW TEST IN ESSEN

3.1 Description of the In-situ Air-Flow Test

An in-situ, air-flow test was carried out by Kramer and Semprich [1] to investigate the air permeability of the Essen soil, determine the extent of the airflow field, and analyze the effect of compressed airflow on the deformation of the soil skeleton and in particular on the surface displacement. Fig. 2 shows a schematic diagram of the experimental setup for the in-situ, air-flow test. According to the description of the related experiment [1], the soil profile in Essen can be divided into the following four distinct layers: a fill layer, a thick silt layer, a thin permeable sand layer and a thick layer of marl that is rather weathered in the upper region and presents pronounced joints. The groundwater table is approximately 4.75 m below the ground surface and is located in the silt layer.

Compressed air can be introduced into the ground through a 1.5-m diameter borehole in the injection well. A thin steel pipe can be installed inside the borehole, the lower part of the pipe being perforated for air permeating into soils and the top of the pipe being connected to an air compressor (which was used to control the air pressure) [1]. In test 1B under consideration here, the

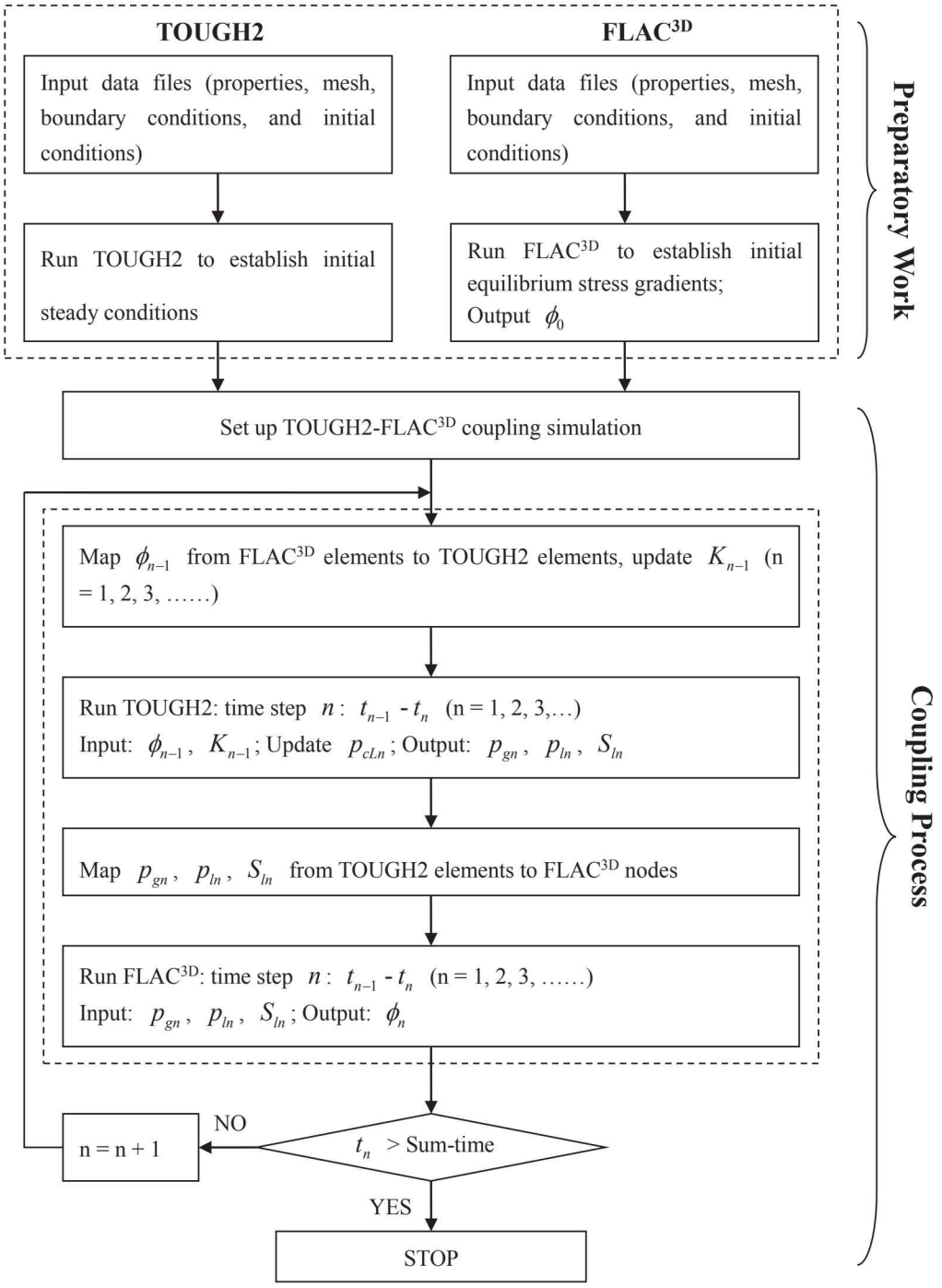

Figure 1. Flow chart for a loosely coupled algorithm.

compressed air was introduced 18.0–21.0 m below the ground surface, and only the first applied pressure level Δp = 160 kPa over 27 h was considered for simplicity. The rate of air injection was monitored by a flow meter during the experiment. Several piezometers were installed near the borehole to measure the variation of the pore pressure at different depths and distances from the borehole. The land uplift was measured by geodetic leveling installed at different distances from the borehole.

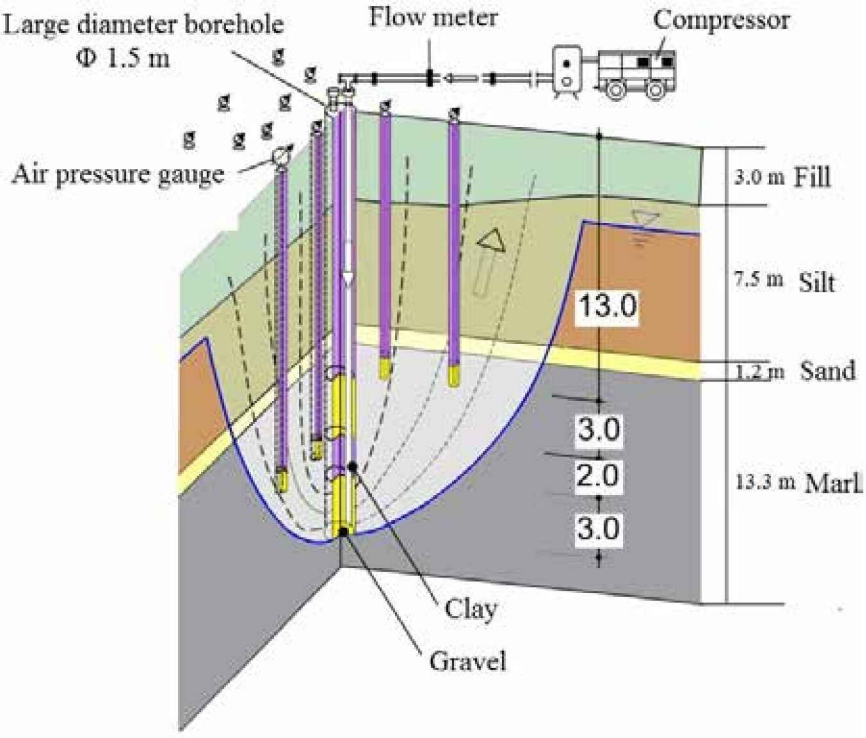

Figure 2. In-situ, air-flow test in Essen (after Kramer and Semprich [1]).

3.2 Setting up of the Numerical Model

3.2.1 Model Domain and Soil Parameters

In this study, the numerical model of the in-situ, air-flow test was established using the above coupling algorithm. Taking advantage of the axial symmetry of this problem, only one-fourth of the domain was simulated. The measured results show that the land uplift reached only 2 mm at approximately 20 m distance from the borehole. The extent of the model was just 40 m in the horizontal direction in the simulation by Öttl [25] and 100 m by Chinkulkijniwat et al. [2]. Therefore, the model domain was 100 m long in both the transverse direction (X) and the longitudinal direction (Y), and was 25 m deep in the vertical direction (Z). The mesh generation in TOUGH2 was the same as in FLAC^{3D}, consisting of 18,259 hexahedron elements and 20,480 nodes, and is shown in Fig. 3. The domain in the vertical direction was discretized to take into account the soil layers, the groundwater table and the air-injection region. The mesh size in the horizontal directions was relatively fine near the borehole and expanded with the distance from the borehole.

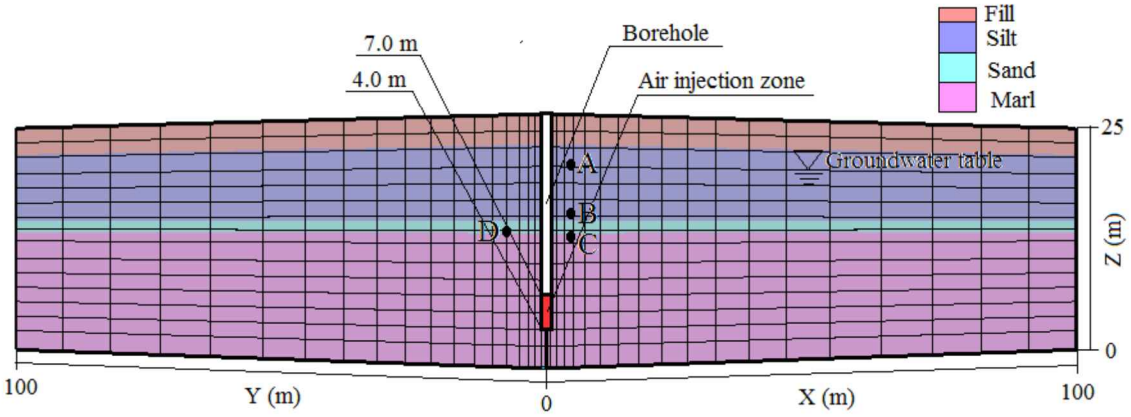

Figure 3. Meshes in the model of TOUGH2 and FLAC^{3D}.

In the numerical simulation, the capillary pressure and the relative liquid and gas permeability dependent on the liquid saturation were described by the van Genuchten model [26] and the van Genuchten-Mualem model [26-27], respectively. The expressions of these two models are described in Eq. (7), Eq. (8) and Eq. (9)

$$p_c = -p_0\left[(S^*)^{-1/\lambda} - 1\right]^{1-\lambda} \qquad (-p_{\max} \le p_c \le 0) \qquad (7)$$

where p_0 is the air entry pressure, λ is a model parameter associated with the degree of soil uniformity, S^* is the effective liquid saturation, $S^* = (S_l - S_{lr}) / (S_{ls} - S_{lr})$, S_l is the liquid saturation, S_{lr} is the residual liquid saturation, and S_{ls} is the saturated liquid saturation.

$$k_{rl} = \begin{cases} S^*\left[1-\left(1-\left(S^*\right)^{1/\lambda}\right)^{\lambda}\right]^2 & (S_l < S_{ls}) \\ 1 & (S_l \ge S_{ls}) \end{cases} \qquad (8)$$

$$k_{rg} = \begin{cases} 1-k_{rl} & (S_{gr} = 0) \\ (1-\hat{S})^2(1-\hat{S}^2) & (S_{gr} > 0) \end{cases} \qquad (9)$$

where $\hat{S} = (S_l - S_{lr}) / (1 - S_{lr} - S_{gr})$ and S_{gr} is the residual gas saturation.

The hydraulic and geo-mechanical parameters for four soil layers in Essen, taken from Ottl [25], are shown in Table 1, including the solid density ρ_s, Young's modulus E, Poisson's ratio v, the initial porosity ϕ_0, the initial intrinsic permeability K_0, p_0, S_{lr}, S_{ls} and λ. Notice that the lower part of the silt layer is characterized by a weaker stiffness. Additionally, due to the rather small deformation occurring in the soil (a maximum value of the measured heave is approximately 4 mm) in the field test, linear elastic behavior was assumed for the whole domain. This assumption of linear elastic behavior has also been used in other simulations of the airflow test in Essen [2, 25]. All the processes involved in the numerical simulation were assumed to occur isothermally at 10°C.

3.2.2 Boundary and Initial Conditions

In TOUGH2, the primary variables are P_β (the pressure of the β phase (the liquid phase (l) or gas phase (g))); X^a_β (the air-mass fraction in the β phase); and T (temperature) for single-phase conditions and P_g, S_g+10 (the gas saturation plus 10) and T for two-phase conditions. The atmospheric boundary conditions, $P_g = p_{atm}$ (where p_{atm} is the atmospheric pressure and was equal to 1.013×10^5 pa), $X^a_\beta = 0.999$, and $T = 10$°C, were applied at the ground surface. The Dirichlet boundary conditions, $P_l = p_{atm} + \rho_w g(20.25 - Z)$, $X^a_l = 1.0\times10^{-10}$, and $T = 10$°C, were applied at the bottom of the domain, where the water density ρ_w was 1000 kg/m^3, the gravitational acceleration g was 9.81 m/s^2, and Z was the elevation of the model domain. No flow boundaries were considered at the lateral boundaries. The initial steady condition was obtained by running TOUGH2 with the above boundary conditions and the initial liquid-saturated condition for a sufficient simulation time until reaching a steady state.

In FLAC^{3D}, the domain surface was specified as a free deformed boundary, whereas no deformation at the bottom of the domain was allowed, i.e., $u_h = 0$ and $u_v = 0$, where u_h is the horizontal displacement and u_v is the vertical displacement. The roller displacement boundary ($u_h = 0$) was prescribed at all the lateral boundaries. Under gravitational loads, the initial steady conditions in TOUGH2 were sent to FLAC^{3D} to calculate the equilibrium stress distribution that was used as the initial conditions for the FLAC^{3D} model. This calculation was the first coupling of the TOUGH2 model with the FLAC^{3D} model.

Then, using the steady conditions of the TOUGH2 model and FLAC^{3D} model as the initial conditions, the material properties of the elements within the injection zone were set as freely movable, and the volume and primary variables of these elements were changed to be infinite and $P_g = p_{atm} + \Delta p$, $X^a_\beta = 0.999$, $T = 10$°C. Because the borehole above the injection zone was impervious in the test, the elements within the borehole were removed in

Table 1. Hydraulic and geo-mechanical parameters for four soil layers in Essen (the values of E and v between parentheses refer to the lower point of the silty layer).

Soil Texture	ρ_s, (g/cm^3)	E (Mpa)	v	ϕ_0	ϕ_0 (kN/m^2)	S_{ls}	S_{lr}	λ	K_0 (10^{-12} m^2)
Fill	2.72	20	0.33	0.36	4.0	0.2	1.0	0.8	4.95
Silt	2.90	12.47	0.35	0.42	30.0	0.2	1.0	0.5	0.495
		(9.24)	(0.37)						
Sand	2.72	21.22	0.32	0.36	4.0	0.05	1.0	0.65	9.90
Marl	2.79	14.33	0.40	0.33	12.0	0.15	1.0	0.6	2.48

the simulations. Then, the coupled hydraulic-mechanical process, considering the interactions between the liquid, gas and solid phases, was repeated until the injection duration of 27 h was reached. Hereafter, the material property and the volume of the elements within the injection zone were reset as the property of the marl and their actual volume, respectively, in order to investigate the variations of multiphase flow and soil deformation after the air injection stopped. The post-injection phase lasted for 100 hours. Notably, the experimental data were not recorded after the air injection stopped in the in-situ, air-flow test.

3.3 Analysis of the Experimental and Simulated Results

3.3.1 Analysis of the Discrepancy between the Simulated and Measured Results

The main objective of this field test is to investigate the magnitude and scope of the land uplift as well as the air loss rate induced by compressed air injection. Fig. 4a shows the distribution of the simulated and measured land uplift at different times. After 27 hours, the simulated land uplift was much higher than the measured value at a distance from the borehole, which might be because the high permeability of the sand layer promoted radial propagation of the overpressure in the numerical simulation. Actually, according to Kramer and Semprich [1] and Ottl [25], the thin sand layer contains a considerable portion of silt in the field, reducing the permeability of the sand layer. Additionally, average values of the permeability for the marl layer were used in the above simulation, although the marl corresponds to silt containing high portions of sand and clay according to Kramer and Semprich [1]. Therefore, the possibility of high anisotropy between the horizontal and vertical soil permeability should be recognized. Fig. 4b compares the behavior over time of the measured and simulated air-injection rates during the test. The mass flux of air (unit: kg/s) injected into the soil interior through the injection zone was calculated using the numerical model and the air density under the normal conditions of atmospheric pressure and 10°C was determined by the ideal gas law, which permitted a calculation of the volume flux of air (m^3/min) injected into the soil. The simulated rate was substantially the same as the measured results during the middle period, whereas there were large differences between them at the initial and final stages. In the field test, the applied air pressure was increased stepwise to 160 kPa by the compressor, as shown in Fig. 5. Before the air pressure reached 160 kPa, the matric suction in the marl layer could not surpass the air entry value of the marl, and no air penetrated into the soil. However, the applied air pressure was set

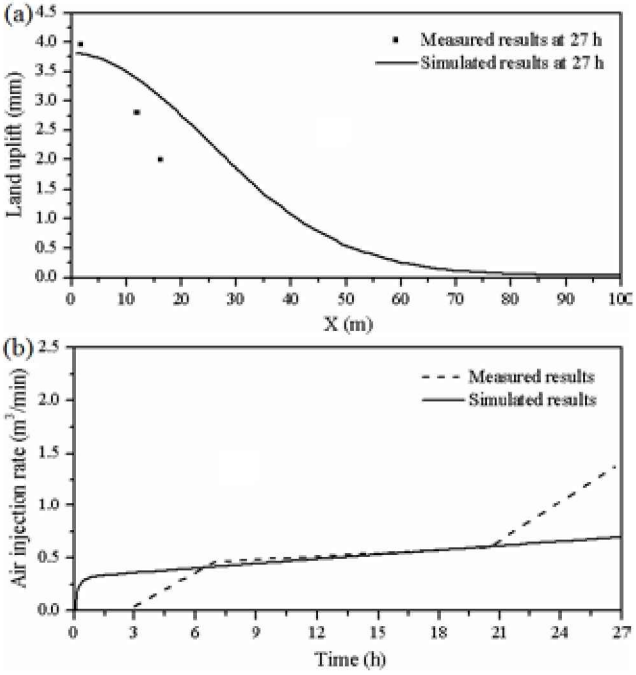

Figure 4. (a) Measured and simulated land uplift at different times and (b) temporal evolution of the simulated and measured air-injection rate during compressed air injection.

to 160 kPa at the beginning of the numerical simulation, so the difference between the measured and simulated results was introduced at the initial stage.

Considering the low permeability of the sand layer, the anisotropy between the horizontal and vertical soil permeability of the marl layer, and the implementation process of the applied air pressure, the values of permeability in the sand and marl layer in the numerical simulations were adjusted as follows: $K_x = K_y = K_z = 0.9\times10^{-12}$ m^2 for the sand layer and $K_x = K_y = 5.58\times10^{-12}$ m^2, $K_z = 3.38\times10^{-12}$ m^2 for the marl layer, and the applied pressure

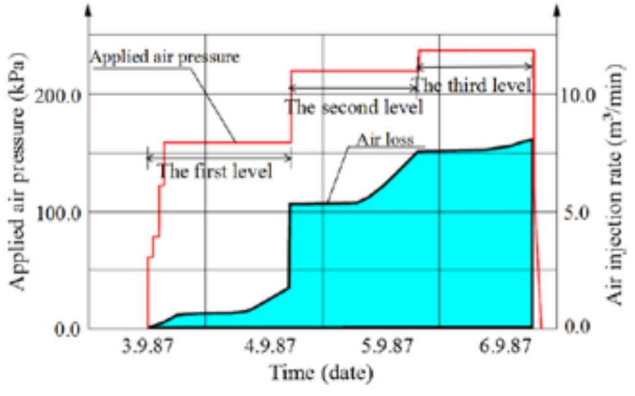

Figure 5. Applied air pressure and air loss versus time for test 1B (after Ottl [25]).

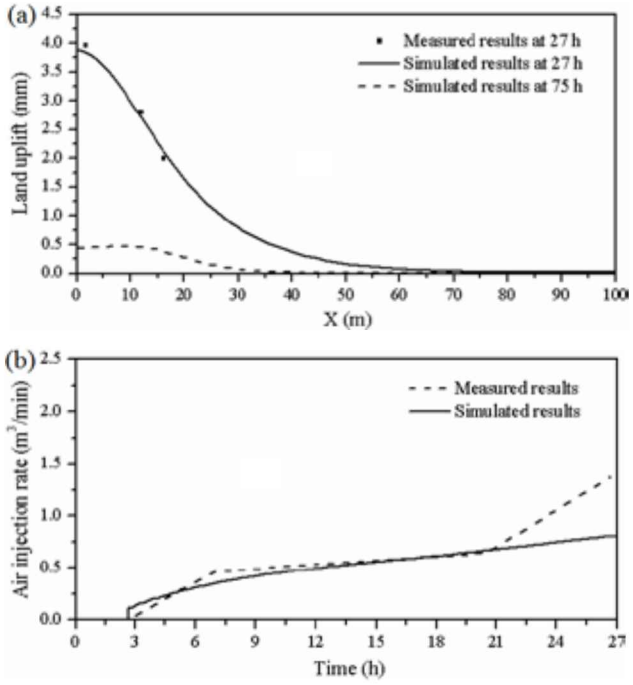

Figure 6. Measured and adjusted simulated land uplift at different times and (b) temporal evolution of the measured and adjusted simulated air-injection rate during compressed air injection.

Δp in the numerical simulations was set as shown in Fig. 5, as follows: Δp = 61 kPa from 0 s to 3360 s, Δp = 78 kPa from 3360 s to 6720 s, Δp = 119 kPa from 6720 s to 10,080 s and Δp = 160 kPa from 10,080 s to 27 hours. The comparison of the adjusted simulated results and the measured results is shown in Fig. 6. There was good agreement between the adjusted simulated and measured land uplift after 27 hours (Fig. 6a). As shown in Fig. 6b, before the air pressure reached 160 kPa (the first 2.8 hours), both the simulated and measured injection rate remained zero. Hereafter, there was a slight discrepancy between the simulated and measured results from 2.8 h to 13 h, whereas they were substantially consistent from 13 h to 21 h. After 21 h, because the air flowed to the location where fractures can be present, the measured rate increased significantly. However, the medium in the numerical model was assumed to be porous media, thereby causing the difference between the simulated and measured rates. In general, the adjusted simulated results agreed well with the measured values, and the adjusted scheme was applied in the following simulation analysis.

3.3.2 Analysis of Seepage and Soil Deformation

Fig. 7a shows the distribution of the simulated gas saturation and airflow after 27 hours. It was expected that the injecting air would permeate into soils due to the pressure gradient and the adjacent regions became unsaturated. Moreover, because the applied air pressure was slightly greater than the maximum groundwater pressure within the air-injection regions, a small area below the injection regions also became unsaturated. The unsaturated zone was concentrated mainly above the air-injection regions. Close to the ground surface, the gas saturation near the borehole decreased because the airflow pushing caused the water to flow upwards. Fig. 7b shows the distribution of gas saturation and air flow after 75 hours (48 hours after compressed air injection stopped). As shown, after the compressed-air injection stopped, the air still flowed upwards and laterally due to the density difference and the pressure gradient, but the magnitude of the air velocity was much smaller at 75 hours than it was at 27 hours. The zone from the bottom to 10 m recovered water saturated because the air in the voids of the injection regions was displaced by the adjacent groundwater, whereas due to the continuous upward airflow, the size of the unsaturated zone from 10 m to 15 m remained substantially unchanged, and from 15 m to the water table, the unsaturated zone expanded into the shallow unsaturated zone.

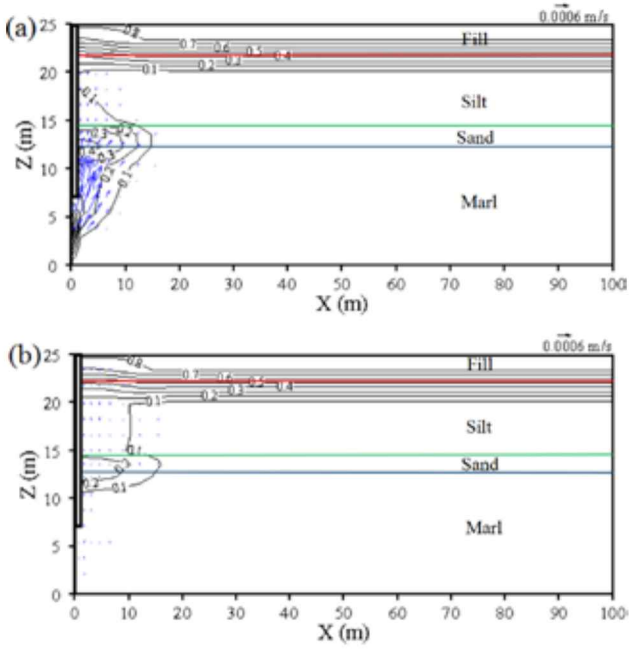

Figure 7. Distribution of simulated gas saturation and airflow at (a) 27 h and (b) 75 h (The blue arrows refer to the magnitude and direction of airflow velocity).

Fig. 8 shows the distribution of the simulated average pore-pressure equivalence at different times. After 27 hours, the average pore pressure near and above the injection zone increased significantly, and the

amplification decreased with the distance from the borehole. The affected zone extended to approximately 70 m horizontally. After 75 hours, due to the airflow dissipation, the average pore pressure near and above the injection zone decreased substantially. From the bottom to approximately 7 m, the average pore pressure recovered to its initial steady value. From 7 m to 16 m, the average pore pressure also decreased to its initial values near the borehole, while it still deviated from the initial values at a distance from the borehole. The reason might be that the gas saturation in this region reached a relatively large value within 10 m horizontally (Fig. 7b), so that it was easy for the airflow to move, but the overpressure and airflow 10 m away dissipated with relative difficulty due to its small gas saturation. Above the elevation of 16 m, the average pore pressure did not decrease to its initial value due to airflow pushing (Fig. 7b). The measured and simulated pore air pressure at the four observed points of A, B, C and D (Fig. 3) are shown in Table 2, and the measured and simulated results were substantially consistent.

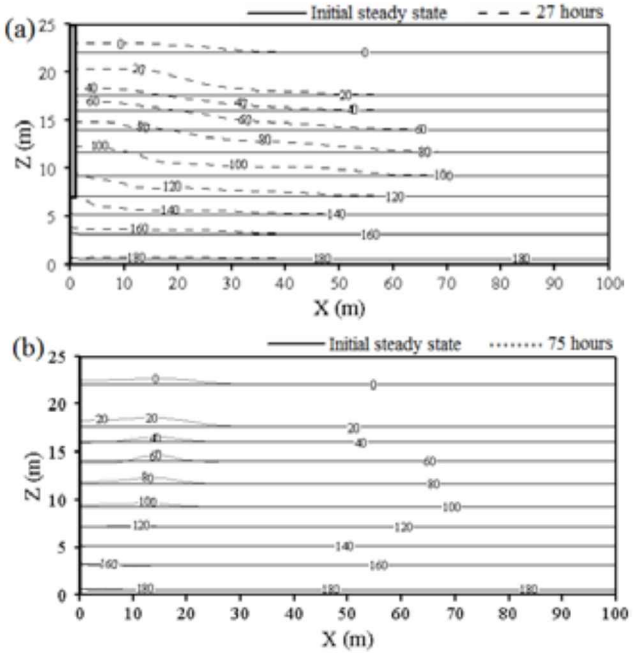

Figure 8. Distribution of simulated average pore pressure at different times at (a) initiation and at 27 h and (b) initiation and at 75 h (unit: kPa).

Table 2. Locations with the measured and simulated pore air pressure for four observation points.

Observation points	A	B	C	D
Horizontal distance from borehole (m)	2	2	2	6
Depth below ground surface (m)	6	10	13	12.5
Measured pore water pressure (kPa)	27	70	95	90
Simulated pore water pressure (kPa)	30.5	76.5	101	95

Fig. 9 shows the distribution of the simulated vertical effective stress at different times. After 27 hours, since the total stress acting on the soil layers remained almost unchanged (the mass of the injected compressed air was very small relative to the weight of the whole soil layers) and the stress overtaken by the fluids in the soil voids increased (Fig. 8), the stress overtaken by the solid skeleton decreased; i.e., the effective stress near and above the injection zones decreased. This release of the vertical effective stress caused an expansion of the soil skeleton in the corresponding zone. The magnitude of the porosity near and above the injection zones therefore increased, and the affected zone of the porosity increment reached approximately 32 m horizontally (Fig. 10a). After 75 hours, the vertical effective stress decreased to its initial values in most areas, while it still appeared to deviate from 12 m to 20 m vertically. Therefore, both the magnitude and scope of the porosity increments also decreased at 75 hours (Fig. 10b), and the maximum value appeared from 10 m to 20 m horizontally due to the distribution of the average pore pressure and vertical effective stress (Figs. 8b and 9).

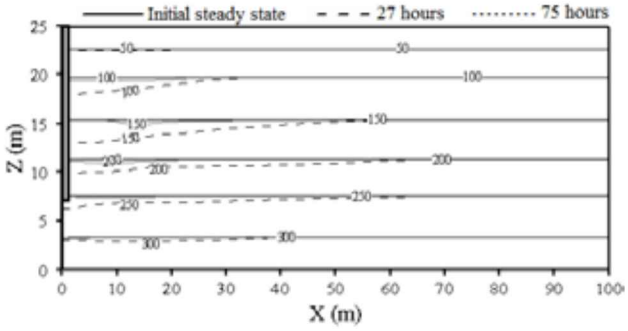

Figure 9. Distribution of simulated vertical effective stress at different times (unit: kPa).

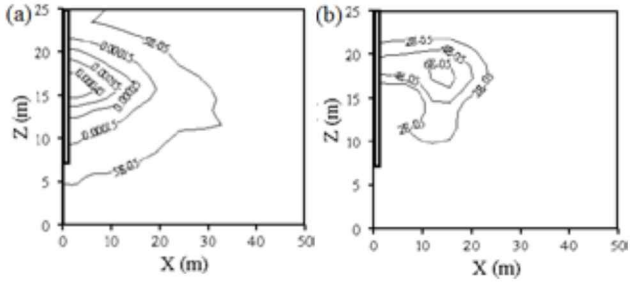

Figure 10. Distribution of the simulated porosity increment at (a) 27 h and (b) 75 h.

Because the porosity near the ground surface changed little, the land uplift was caused primarily by the expansion of deep deformed soils. As shown in Fig. 6a, after 27 hours, the maximum land uplift occurred near the borehole. The land uplift decreased with the distance from the borehole, consistent with the distribution of

the porosity increment within the soil. After 75 hours, the land uplift decreased due to overpressure dissipation and the flat segment within approximately 15 m from the borehole was relevant to the distribution of the porosity increment at 75 h. Fig. 11 shows the behavior over time of the maximum land uplift. During compressed air injection, the land uplift remained zero before 2.8 hours due to no air penetrating into the soil. Later, it increased rapidly and reached a maximum value at 27 hours. After the injection stop, the heave decreased rapidly at first and then gradually went to zero at approximately 110 hours.

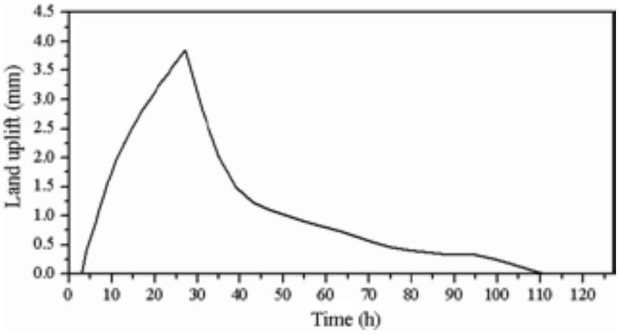

Figure 11. Time behavior of the maximum land uplift.

4. ANALYSIS OF THE IMPACTS OF DIFFERENT FACTORS

4.1 Rain Events

To investigate the effects of a rain event on multiphase flow and land uplift during and after compressed-air injection, rain with intensity equal to 5 mm/h and 20 mm/h was combined with the compressed-air injection. Notably, the duration of rainfall coincided with that of the applied pressure of 160 kPa (i.e., 2.8–27 hours). The model source term in kg/s for rainfall is computed as $m(t) = r_w A_e Q_r(t)$, where t (s) is the time; A_e (m^2) is the effective area for rainwater infiltration and is equal to the area perpendicular to the direction of rainfall; and Q_r (m/s) is the rainfall intensity. The term was applied to the whole soil surface (i.e., the soil elements adjacent to the atmospheric boundary). As the compressed air injection and rainfall stopped, the source term was removed. The whole simulation time, the initial conditions and the other boundary conditions were the same as the base case.

Fig. 12 shows the total stress distribution for different profiles at 27 h for the three cases. The total stress for different profiles after 27 h for the three cases was essentially consistent with that at the initial steady state, indicating that the applied rainwater amount has

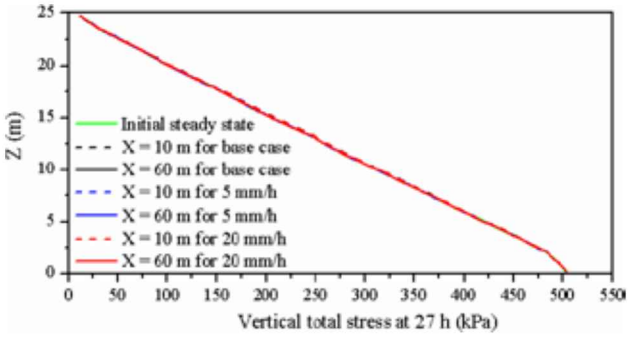

Figure 12. Distribution of total stress for different profiles at 27 h for the base case and rain intensities of 5 mm/h and 20 mm/h.

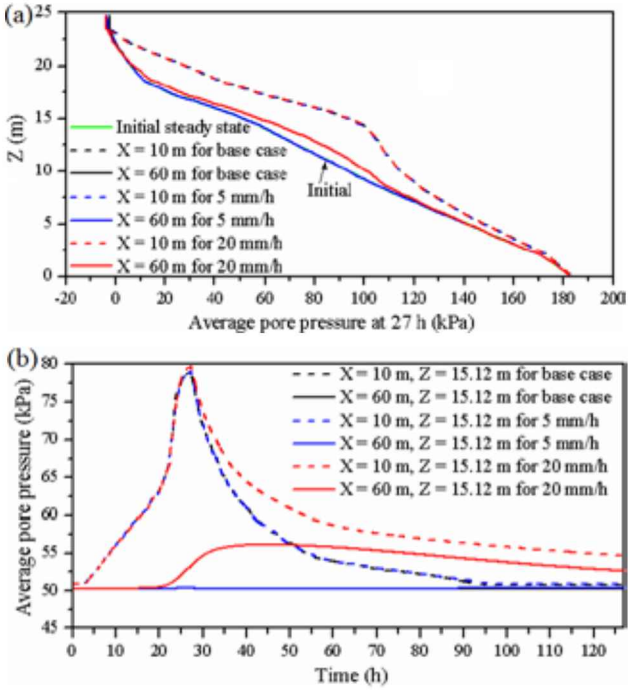

Figure 13. (a) Distribution of the average pore pressure for different profiles at 27 h and (b) the temporal evolution of the average pore pressure at different points for the base case and rain intensities of 5 mm/h and 20 mm/h.

little effect on the total stress. The intensive rainfall produced a continued downward wetting front, which reduced the escape of pore air and compressed pore air between the wetting front and the capillary fringe. As a result, the pore pressure in the unsaturated and saturated zones increased due to airflow pushing by the advancing wetting front. However, a small amount of rainfall cannot completely seal off the ground surface, and pore air could partially escape out of the surface during rainfall and it cannot be compressed and pressurized by the moving wetting front. As shown in Fig. 13a, the average pore pressure distribution for X = 10 m

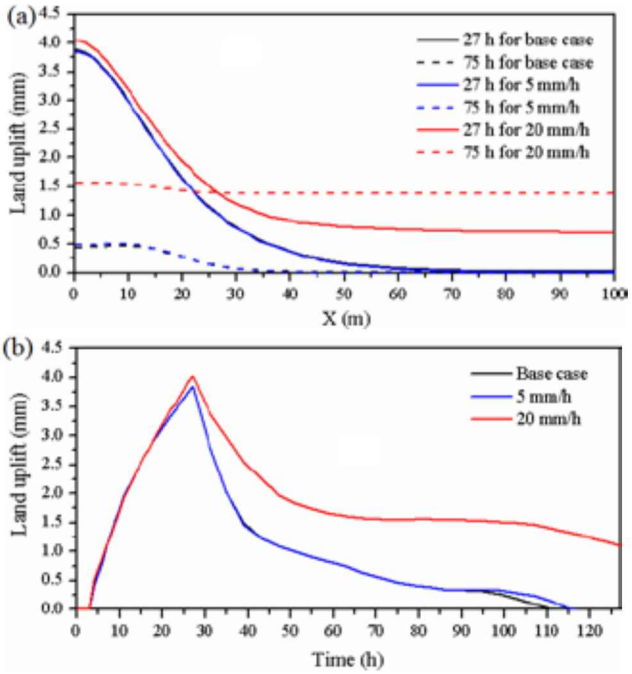

Figure 14. (a) Land uplift at different times and (b) changes in the maximum land uplift with time for the base case and rain intensity of 5 mm/h and 20 mm/h.

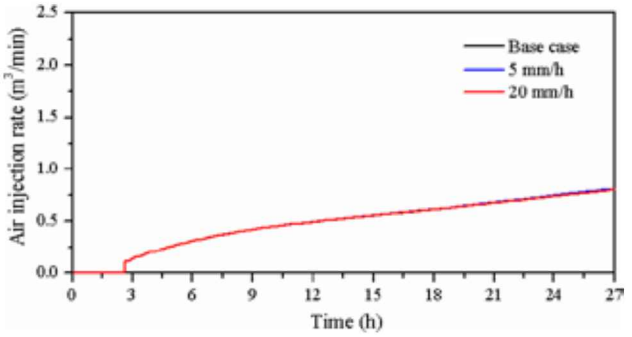

Figure 15. Temporal evolution of the air-injection rate for the base case and rain intensities of 5 mm/h and 20 mm/h during compressed-air injection.

at 27 h seemed to be mostly identical for the three cases, and all deviated from their initial values. The average pore pressure distributions for X = 60 m remained at their initial values for the base case and rain intensity of 5 mm/h, but they deviated from the initial state vertically from approximately 8 m to 20 m for a rain intensity of 20 mm/h. Likewise, as seen in Fig. 13b, the time evolution of the average pore pressure at points ((X = 10 m, Z = 15.12 m) and (X = 60 m, Z = 15.12 m)) was also almost identical for the base case and 5 mm/h, while it began to deviate from the variation of the above two cases at different times for 20 mm/h. Moreover, the magnitude of this deviation was smaller for X = 10 m than for X = 60 m (notably, the seemingly identical pore pressure for X = 10 m at 27 h for three cases in Fig. 13a was limited by the adopted coordinate range). As a result, the distribution of land uplift at 27 h for 5 mm/h was substantially the same as the base case, while the magnitude of the land uplift for 20 mm/h was slightly greater near the borehole, but was much greater at a distance from the borehole than that for the other cases (Fig. 14a). This phenomenon suggested that a low rain intensity (i.e., 5 mm/h in this case) hardly affected the land uplift induced by compressed-air injection, but a high rain intensity (i.e., 20 mm/h in this case) would elevate this land uplift to different levels at different positions. Additionally, as shown in Fig. 14b, it was expected that the maximum land uplift for 5 mm/h was almost consistent with the base case, except that the time required for the 5 mm/h uplift to reach zero was slightly delayed. However, the land uplift for a rain intensity of 20 mm/h began to deviate from the base-case solution at 23 hours, consistent with the variation of the pore pressure (Fig. 13b), probably because the increasing pore pressure induced by intensive rainfall needed some time. Hereafter, the land uplift for 20 mm/h decreased gradually, but its value did not reach zero at the end of the simulation period due to the increasing pore pressure.

Fig. 15 shows the time evolution of the air-injection rate for the base case, rain intensity of 5 mm/h, and 20 mm/h during compressed-air injection. The behavior of the air-injection rate was almost the same for the three cases, probably because the changes in pore pressure near the injection zone were essentially identical for the three cases (Fig. 13a).

4.2 Permeability of Injected Strata

The permeability of the injection zone reflects the ability of soils to conduct water and air, and it plays an important role in the permeation of compressed air into the soil. Different values were considered for the intrinsic permeability of the marl layer (i.e., the injected strata), 0.5 K_{base}, K_{base} and 1.5 K_{base}, to analyze its effects on the multiphase flow and land lift during and after compressed air injection. Notably, K_{base} represented the adjusted intrinsic permeability of the marl layer in three directions (X, Y and Z). All the other simulation conditions were the same as those for the base case.

A large permeability promoted the injected air to flow into the soil voids and affected the seepage and soil deformation in the aquifer. Therefore, as shown in Fig. 16a, with a large permeability, the land uplift increased

at 27 hours. However, at 75 h, the land uplift near the borehole was substantially the same with a different permeability, probably because the unsaturated zone in this region was connected to the shallow unsaturated zones and the dissipation of the overpressure was almost the same. Additionally, the varying rate and the maximum value of the maximum land uplift also increased with increasing permeability during the compressed-air injection. Hereafter, the land uplift with a different permeability decreased gradually to zero, but the time required to reach zero was slightly advanced with a small permeability (Fig. 16b). Similarly, the air-injection rate through the injection section also increased as the permeability of the injected strata increased (Fig. 17).

4.3 Air Entry Pressure of Injected Strata

The air entry pressure denotes the matric suction at which air begins to enter into the maximum pore space of the soils, and it is an important parameter in the soil-water characteristic curve. It is easier for air to permeate soils with a lower air entry pressure (coarse materials). Three different values were considered for the air entry pressure of the injected strata, i.e., 0.5 p_{base} , p_{base} (base case) and 1.5 p_{base} . Notably, p_{base} was the air entry pressure of the marl layer in the base case (Table 1). The other simulation conditions were the same as those for the base case.

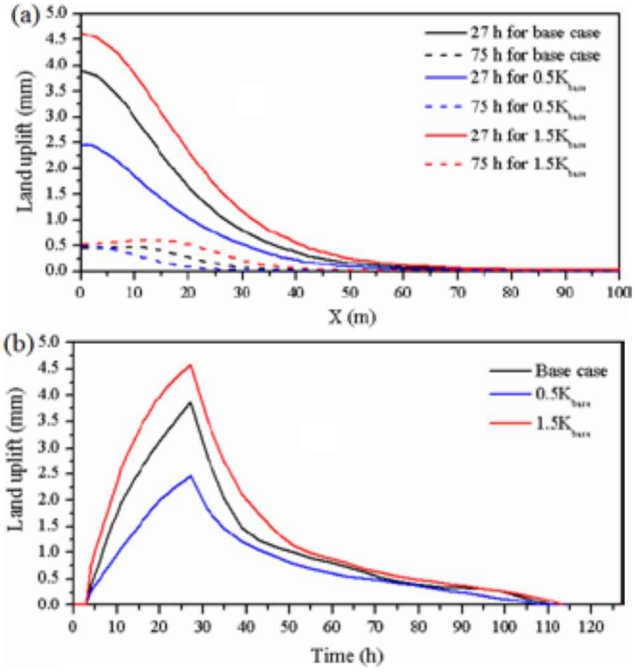

Figure 16. (a) Land uplift at different times and (b) changes in the maximum land uplift with time for different permeabilities.

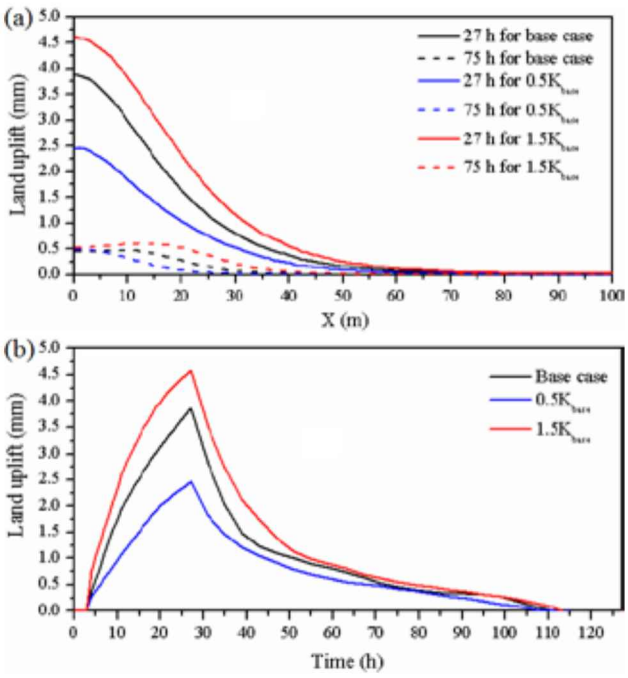

Figure 18. (a) Land uplift at different times and (b) changes in the maximum land uplift with time for different air entry pressures.

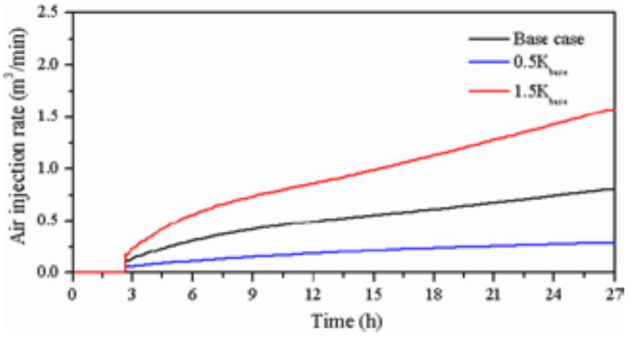

Figure 17. Temporal evolution of the air-injection rate for different permeabilities during compressed air injection.

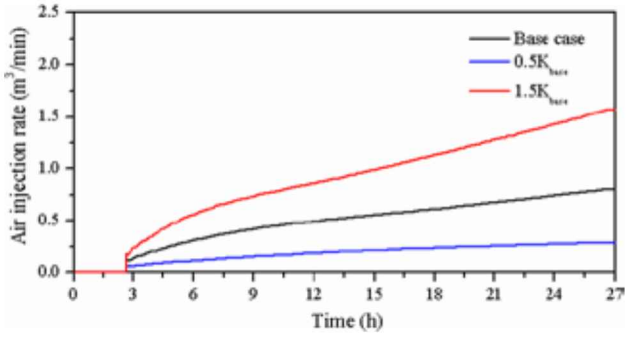

Figure 19. Temporal evolution of the air loss rate for different air entry pressures during compressed-air injection.

As shown in Fig. 18a, with decreasing air entry pressure, the land uplift increased at 27 h, but it varied at different positions at 75 h. Additionally, the varying rate and the maximum value of the maximum land uplift increased with the air entry pressure decreasing during air injection, but the variation of the dissipation of land uplift was similar with different air entry pressures, and the time when the land uplift reached zero was slightly advanced with a high air entry pressure (Fig. 18b). Additionally, the air injection rate increased with decreasing air entry pressure (Fig. 19).

5 SUMMARY AND CONCLUSIONS

In this study, a loosely coupled two-phase flow and geo-mechanical model approach linking two numerical codes, TOUGH2/EOS3 and FLAC^{3D}, was used to investigate the interaction between multiphase flow and soil skeleton deformation underground. Owing the air-flow test in Essen, the effect of different factors on seepage and soil deformation during and after the compressed-air injection was investigated using this coupled model.

As compressed air is injected into the soil layer, the air mainly flows upwards and laterally and the adjacent regions become unsaturated. The average pore pressure and the vertical effective stress near and above the injection zones increases and decreases, respectively, causing the porosity in the corresponding zone to increase. After the termination of the compressed-air injection, both the magnitude and the scope of the porosity increments decrease due to overpressure dissipation. The land uplift, caused primarily by the expansion of the deep layers, reaches the maximum value at the end of the injection phase, and then it decreases to zero after a certain period.

When a rain event, imposed at the ground surface, is combined with air injection underground, the seepage and soil deformation presents a complex response. If the rain intensity is too low to completely seal off the ground surface, the pore air in the unsaturated zones can easily escape out of the ground surface during rainfall, and the land uplift is substantially the same as the base case. However, if the rain intensity is so great that the pore air in unsaturated zones cannot flow easily back to the atmosphere during rainfall and is compressed by the advancing wetting front, the pore pressure in the unsaturated and saturated zones increases, causing the magnitude of the land uplift to increase, but this difference is relatively small near the borehole. Nevertheless, the air-injection rate through the injection section is scarcely affected by a rain event (high or low ran intensity). When the intrinsic permeability increases or the air entry pressure decreases in the injected strata, both the land uplift and the air injection rate through the injection section increase during air injection, but the time required for the land uplift to reach zero is slightly advanced with a small permeability or a high air entry pressure. Therefore, with regard to some scenarios of subsurface fluid injection, a detailed and meticulous strata exploration is required, and the soil properties can significantly affect the multiphase flow and soil deformation during fluid injection. Meanwhile, for different purposes, different strata should be chosen for injecting fluids. Additionally, as a fluid displaces another fluid in porous media, the front is usually perturbed owing to the difference in the physical properties of the fluids, for instance, viscosity, density, surface tension or permeability across the interface of two fluids, thereby causing the development of a fingering phenomenon [28-29]. Therefore, further work needs to be performed to develop a more advanced numerical model to consider the development of fingering during the process of air displacing water.

Acknowledgments

This work was supported by the National Nature Science Foundation of China (Grant NO. 51579170 and 51179118) and the Science Fund for Creative Research Groups of the National Natural Science Foundation of China (Grant No. 51321065).

REFERENCES

[1] Kramer, J., Semprich, S. 1989. E Erfahrungen über Druckluftverbrauch bei der Spritzbetonbauweise (in German). Taschenbuch für den Tunnelbau 13, 91-153.

[2] Chinkulkijniwat, A., Horpibulsuk, S., Semprich, S. 2014. Modeling of Coupled Mechanical–Hydrological Processes in Compressed-Air-Assisted Tunneling in Unconsolidated Sediments. Transport in Porous Media 108, 1, 105-129. DOI: 10.1007/s11242-014-0295-6

[3] Selvadurai, A.P.S. 2006. Gravity-driven advective transport during deep geological disposal of contaminants. Geophysical Research Letters 33, L08408. DOI: 10.1029/2006GL025944

[4] Wong, R.C.K., Lau, J. 2008. Surface heave induced by steam stimulation in oil sand reservoirs. Journal of Canadian Petroleum Technology 47, 01, 13-17. DOI: 10.2118/08-01-13-TN

[5] Teatini, P., Gambolati, G., Ferronato, M., Settari, A.T., Walters, D. 2011. Land uplift due to subsurface fluid injection. Journal of Geodynamics 51, 1, 1-16. DOI: 10.1016/j.jog.2010.06.001

[6] Rutqvist, J. 2012. The geomechanics of CO_2 storage in deep sedimentary formations. Geotechnical and Geological Engineering 30, 3, 525-551. DOI: 10.1007/s10706-011-9491-0

[7] Selvadurai, A.P.S. 2009. Heave of a surficial rock layer due to pressures generated by injected fluids. Geophysical Research Letters 36, 14. DOI: 10.1029/2009GL038187

[8] Rutqvist, J., Vasco, D.W., Myer, L. 2010. Coupled reservoir-geomechanical analysis of CO_2 injection and ground deformations at In Salah, Algeria. International Journal of Greenhouse Gas Control 4, 2, 225-230. DOI: 10.1016/j.ijggc.2009.10.017

[9] Kim, J., Selvadurai, A.P.S. 2015. Ground heave due to line injection sources. Geomechanics for Energy and the Environment 2, 1-14. DOI: 10.1016/j.gete.2015.03.001

[10] Selvadurai, A.P.S., Kim, J. 2015. Ground subsidence due to uniform fluid extraction over a circular region within an aquifer. Advances in Water Resources 78, 50-59. DOI: 10.1016/j.advwatres.2015.01.015

[11] Selvadurai, A.P.S., Kim, J. 2016. Poromechanical behaviour of a surficial geological barrier during fluid injection into an underlying poroelastic storage formation. Proc. R. Soc. A. The Royal Society 472, 2187: 20150418. DOI: 10.1098/rspa.2015.0418

[12] Pruess, K., Oldenburg, C., Moridis, G. 1999. TOUGH2 User's Guide Version 2.0. University of California, Berkeley, USA.

[13] ITASCA Consulting Group Inc. 2002. Fast Lagrangian Analysis of Continua in 3 Dimensions Version 2.10, User's Manual. ITASCA Consulting Group Inc, Minnesota.

[14] Rutqvist, J., Wu, Y.S., Tsang, C.F., Bodvarsson, G. 2002. A modeling approach for analysis of coupled multiphase fluid flow, heat transfer, and deformation in fractured porous rock. International Journal of Rock Mechanics and Mining Sciences 39, 429-442. DOI: 10.1016/S1365-1609(02)00022-9

[15] Rutqvist, J., Tsang, C.F. 2003. TOUGH-FLAC: a numerical simulator for analysis of coupled thermal-hydrologic-mechanical processes in fractured and porous geological media under multi-phase flow conditions. In Proceedings of the TOUGH Symposium 12-14.

[16] Rutqvist, J., Bäckström, A., Chijimatsu, M., Feng, X.T., Pan, P.Z., Hudson, J., Jing, L., Kobayashi, A., Koyama, T., Lee, H.-S., Huang, X.-H., Rinne, M., Shen, B. 2009. A multiple-code simulation study of the long-term EDZ evolution of geological nuclear waste repositories. Environmental geology 57, 6, 1313-1324. DOI: 10.1007/s00254-008-1536-1

[17] Rutqvist, J. 2008. Analysis of injection-induced micro-earthquakes in a geothermal steam reservoir, the Geysers Geothermal Field, California. Lawrence Berkeley National Laboratory.

[18] Rutqvist, J., Moridis, G. J. 2007. Numerical studies on the geomechanical stability of hydrate-bearing sediments. In Offshore Technology Conference. Offshore Technology Conference.

[19] Tsang, C. F., Birkholzer, J., Rutqvist, J. 2008. A comparative review of hydrologic issues involved in geologic storage of CO_2 and injection disposal of liquid waste. Environmental Geology 54, 8, 1723-1737. DOI: 10.1007/s00254-007-0949-6

[20] Cappa, F., Rutqvist, J., Yamamoto, K. 2009. Modeling crustal deformation and rupture processes related to upwelling of deep CO_2-rich fluids during the 1965-1967 Matsushiro earthquake swarm in Japan. Journal of Geophysical Research: Solid Earth 114, B10. DOI: 10.1029/2009JB006398

[21] Bear, J., Bachmat, Y. 1990. Introduction to Modeling of Transport Phenomena in Porous Media (Vol. 4). Springer Science & Business Media.

[22] Chapuis, R.P., Aubertin, M. 2003. On the use of the Kozeny Carman equation to predict the hydraulic conductivity of soils. Canadian Geotechnical Journal 40, 3, 616-628. DOI: 10.1139/T03-013

[23] Taylor, D.W. 1948. Fundamentals of soil mechanics. John Wiley & Sons, New York.

[24] Leverett, M.C. 1941. Capillary behavior in porous solids. Transactions of the AIME 142, 152-168. DOI: 10.2118/941152-G

[25] Öttl, G. 2003. A Three-phase FE-model for Dewatering of Soils by Means of Compressed Air. Universität Innsbruck AI: Publik.-Bereich.

[26] Van Genuchten, M.T. 1980. A closed-form equation for predicting the hydraulic conductivity of unsaturated soils, Soil science society of America journal 44, 892-898. DOI: 10.2136/sssaj1980.03615995004400050002x

[27] Mualem, Y. 1976. A new model for predicting the hydraulic conductivity of unsaturated porous media. Water resources research 12, 513-522. DOI: 10.1029/WR012i003p00513

[28] Homsy, G. M. 1987. Viscous fingering in porous media. Annual review of fluid mechanics 19, 1, 271-311. DOI: 10.1146/annurev.fl.19.010187.001415

[29] Moortgat, J. 2016. Viscous and gravitational fingering in multiphase compositional and compressible flow. Advances in Water Resources 89, 53-66. DOI: 10.1016/j.advwatres.2016.01.002